A hybrid thiophene-oxadiazole compound as a potent copper corrosion inhibitor: An integrated SEM, RSM, and DFT investigation

F. Chellali
Laboratory of Catalysis and Organic Synthesis LCSCO, Faculty of Sciences, University Abou bekr Belkaid, Tlemcen, Algeria.

Y. Datoussaid
Laboratory of Catalysis and Organic Synthesis LCSCO, University Abou Bekr Belkaid, Tlemcen , Algeria. Ecole Supérieure en Sciences Appliquées de Tlemcen (ESSAT), Tlemcen, Algeria.

M. Houbad
Mathematics Department, University Abou Bekr Belkaid, Tlemcen, Algeria.

A. Benchadli
Laboratory of Toxicomed, University Abou Bekr Belkaid, Tlemcen, Algeria.

I. Daoud
University Mohamed Khider, Department of Matter Sciences, Biskra, Algeria.

J. A. Seijas and M. P. Vázquez-Tato
Departamento de Quimica Orgánica, Facultade de Ciencias, Universidade de Santiago de Compostela, Campus Terra, 27080 Lugo, Spain.

E. Ilhan
Center for Nanotechnology & Biomaterials Application and Research (NBUAM), Marmara University, Turkey. Department of Bioengineering, Faculty of Engineering, Marmara University, 34722, Turkey

O. Gunduz
Center for Nanotechnology & Biomaterials Application and Research (NBUAM), Marmara University, Turkey. Department of Metallurgical and Materials Engineering, Faculty of Technology, Marmara University, 34722, Turkey.

T. Attar
Ecole Supérieure en Sciences Appliquées de Tlemcen (ESSAT), Tlemcen, Algeria Laboratory of Toxicomed, University Abou Bekr Belkaid, Tlemcen, Algeria.

Received 4 April 2026; accepted 2 June 2026

Corrosion of copper in sulfuric acid environments poses persistent challenges across numerous industrial applications, necessitating the development of effective and mechanistically well-understood inhibitors. This work presents a comprehensive evaluation of 5-(5-(4-nitrophenyl) thiophen-2-yl)-1,3,4-oxadiazole-2(3H)-thione (NPT-OxT) as a corrosion inhibitor for copper immersed in $0.5\,\mathrm{M\,H_2SO_4}$, employing an integrated experimental-computational methodology. Gravimetric measurements, optimized through Response Surface Methodology, yielded exceptional model reliability ($R^2 = 0.999$) and revealed a maximum protection efficiency of 97% under optimized conditions. Thermodynamic analysis of the adsorption process disclosed a dual physisorption-chemisorption character, with Gibbs free energy values between -39.64 and $-40.48\,\mathrm{kJ\cdot mol^{-1}}$, indicative of thermodynamically favorable and robust interfacial binding. Activation energy data further substantiated inhibitor efficacy, rising from $7.36\,\mathrm{kJ\cdot mol^{-1}}$ in uninhibited solution to $40.38\,\mathrm{kJ\cdot mol^{-1}}$ upon NPT-OxT addition, reflecting the formation of a stable protective barrier. Surface morphological examination via SEM confirmed a marked transition from extensive corrosion damage to a uniform, compact film in inhibitor-containing media, while EDX profiling evidenced suppressed oxidation and sulfur incorporation alongside a dominant copper signal. Quantum chemical calculations using DFT revealed a HOMO-LUMO energy gap of $3.084\,\mathrm{eV}$, a negative electron-transfer parameter ($\Delta N = -0.139$), and an electrophilicity index of $7.659\,\mathrm{eV}$, collectively affirming strong electron-donation capacity and favorable adsorption onto copper. These findings establish NPT-OxT as a highly efficient corrosion inhibitor with clear industrial applicability in aggressive acidic conditions.

Keywords: Copper corrosion inhibition; sulfuric acid medium; oxadiazole derivative; response surface methodology; adsorption thermodynamics; surface analysis and energy-dispersive x-ray; density functional theory.

DOI: https://doi.org/10.31349/RevMexFis.72.061001

1. Introduction

Corrosion of metals in acidic environments remains one of the most persistent and costly challenges across industrial sectors. Processes such as metal cleaning, pickling, and descaling rely on strong acids like sulfuric acid, which, while effective in removing oxides and impurities, accelerate the dissolution of metallic substrates [1]. Among susceptible materials, copper is of particular concern. Its outstanding electrical and thermal conductivity make it indispensable in electronics, energy systems, and marine applications [2–4], yet its high reactivity in acidic solutions leads to rapid degradation, efficiency loss, and significant maintenance costs. In sulfuric acid, copper dissolution is further aggravated by the absence of a stable passive layer, rendering protective strategies essential.

Corrosion inhibitors represent one of the most efficient and economical solutions to mitigate acid-driven metal degradation [5]. Even at very low concentrations, these compounds can significantly suppress corrosion by adsorbing onto the metal surface and forming protective layers [6]. Organic inhibitors, in particular, have gained considerable interest because of their structural flexibility and the presence of heteroatoms (N, O, S, P), which enhance surface binding through donor-acceptor interactions, hydrogen bonding, and π-d orbital overlap [7–9]. Within this category, heterocyclic molecules incorporating oxadiazole and thione units stand out due to their electron-rich centers, extended π-conjugation, and strong coordination ability with transition metals. Importantly, inhibitor efficiency is not dictated solely by molecular structure but also by external factors such as temperature, acid concentration, and immersion duration, whose combined influence is often intricate and nonlinear. Numerous investigations have demonstrated that these adsorption mechanisms reduce the accessible surface area for electrochemical reactions, thereby slowing both anodic metal dissolution and cathodic processes.

To rationalize and predict inhibitor efficiency, the integration of computational and statistical tools alongside experimental evaluation has become increasingly important. Density Functional Theory (DFT) provides molecular descriptors such as frontier orbital energies, electronegativity, and hardness/softness indices, which identify reactive sites and predict adsorption tendencies at the metal-solution interface [10]. These insights strengthen mechanistic understanding and support structure-activity correlations. In parallel, Response Surface Methodology (RSM) offers a powerful statistical framework for simultaneously evaluating multiple factors and their interactions, reducing experimental effort while ensuring robust model accuracy [11, 12]. Despite their demonstrated value, relatively few studies have combined DFT with RSM to achieve both molecular-level interpretation and experimental optimization in copper corrosion systems.

In this work, we investigate the corrosion inhibition performance of 5-(5-(4-nitrophenyl) thiophen-2-yl)-1,3,4-oxadiazole-2(3H)-thione (NPT-OxT) on copper in 0.5 M H_2SO_4. Gravimetric measurements, adsorption isotherms, thermodynamic and kinetic analyses, and surface morphology evaluation via SEM were complemented with statistical modeling via RSM and theoretical calculations via DFT. This integrated strategy was designed to (i) determine inhibition efficiency under optimized experimental conditions, (ii) elucidate the adsorption mechanism using quantum chemical descriptors, and (iii) demonstrate the synergy between statistical, computational, and surface analytical approaches in guiding the rational design of efficient corrosion inhibitors. By combining predictive accuracy with mechanistic depth, the present study positions NPT-OxT as a potent candidate for copper protection in acidic environments and highlights the broader potential of RSM-DFT-SEM integration in corrosion science.

2. Material and methods

2.1. Weight loss measurements

To investigate the corrosion behavior of copper in acidic media, weight loss experiments were conducted using a 0.5 M H_2SO_4 solution, prepared by diluting analytical-grade (98%) sulfuric acid with distilled water. Inhibitor solutions were freshly prepared at concentrations of 1.0×10^{-5} to 1.0×10^{-4} M by accurately weighing the required amounts and dissolving them in the corrosive medium, followed by thorough agitation to ensure complete homogenization. High-purity copper specimens (99%) were fabricated into square-shaped discs, polished sequentially using emery papers ranging from 600 to 2000 grit, rinsed with distilled water, degreased in acetone, and dried under a warm air stream. The prepared samples were immersed in 100 mL of test solutions, both in the absence and presence of the inhibitor, for periods ranging from 1 to 3 hours. Temperature-dependent studies were carried out in the range of $293 - 333$ K. After immersion, specimens were re-cleaned, dried, and reweighed. The mass loss was used to determine the corrosion rate, and inhibition efficiency was calculated accordingly. All tests were performed in triplicate to ensure statistical reliability and reproducibility of the results.

The corrosion rate (CR) and inhibition efficiency (IE%) were determined using the following equations [3]:

$$CR = \frac{\Delta m}{S \times t}, \tag{1}$$

$$\text{IE}(\%) = \frac{CR_0 - CR_{\text{inh}}}{CR_0} \times 100, \tag{2}$$

where Δm is the mass loss in grams, S is the surface area of the exposed copper in cm^2, and t is the immersion time in hours. CR_0 and CR_{inh} represent the corrosion rates in the absence and presence of the inhibitor, respectively.

TABLE I. Experimental range and coded levels for corrosion inhibition study.

Factors	Names	Units	Low (-1)	Middle (0)	High (+1)
X_1	Con	$\mathrm{mol \cdot L^{-1}}$	10^{-5}	5.5×10^{-5}	10^{-4}
X_2	Temp	$^{\circ}\mathrm{C}$	20	40	60
X_3	Tim	hours	1	2	3
X_4	Aci	$\mathrm{mol \cdot L^{-1}}$	0.25	0.50	0.75

2.2. Experimental design and optimization

A Response Surface Methodology RSM framework was applied to efficiently design and optimize the corrosion inhibition experiments, reducing the number of required tests while retaining the ability to evaluate both individual and interactive effects of the studied factors.

The design and statistical analysis were carried out using MODDE® 9.1 software, implementing a central composite face-centered CCF design to investigate the influence of four independent variables-inhibitor concentration (X_1), temperature (X_2), immersion time (X_3), and acid concentration (X_4) on the inhibition efficiency (IE%) of an organic inhibitor for copper in 0.5 M H_2SO_4 Each parameter was tested at three coded levels (low = -1, middle = 0, high = +1), as summarized in Table I.

The obtained data were modeled using a second-order polynomial equation, enabling the quantification of linear, quadratic, and interaction terms while accounting for statistical error. This model structure ensured precise estimation of regression coefficients and strong predictive reliability. The inhibition efficiency (Y) was selected as the primary response, described by:

$$Y = a_0 + \sum_i a_i X_i + \sum_i a_{ii} X_i^2 + \sum_{ij} a_{ij} X_i X_j + \varepsilon, \quad (3)$$

where Y is the response matrix, X_i and X_j are the coded independent variables, a_0 is the intercept, a_i, a_{ii} and a_{ij} represent the linear, quadratic, and interaction coefficients, respectively, and ε denotes the random error term. This statistical formulation effectively captured the complex relationships between process variables, allowing reliable optimization of corrosion protection performance.

2.3. Adsorption mechanism and activation energy evaluation

The inhibition mechanism of the organic inhibitor on copper in 0.5 M H_2SO_4 was examined through adsorption isotherm modeling and thermodynamic kinetic parameter analysis. Adsorption refers to the attachment of inhibitor molecules onto the copper surface, forming a compact barrier layer that retards corrosion.

To elucidate the adsorption behavior, surface coverage data ($\theta = \mathrm{IE}/100$), obtained from weight-loss measurements, were fitted to multiple adsorption models: Langmuir, Freundlich, Frumkin, Temkin, Flory-Huggins, and El-Awady. Among these, the Langmuir isotherm which assumes uniform monolayer adsorption was found to provide the most consistent fit [8]:

$$\frac{C_{\text{inh}}}{\theta} = \frac{1}{K_{\text{ads}}} + C_{\text{inh}}, \quad (4)$$

where C_{inh} is the inhibitor concentration ($\mathrm{mol \cdot L^{-1}}$), θ is the fractional surface coverage, and K_{ads} is the adsorption equilibrium constant ($\mathrm{L^{-1}\,mol}$).

The enthalpy of adsorption (ΔH_{ads}) was determined using the van't Hoff relation [8]:

$$\ln(K_{\text{ads}}) = -\frac{\Delta H_{\text{ads}}}{RT} + \mathrm{Const.} \quad (5)$$

The Gibbs free energy of adsorption (ΔG_{ads}) was calculated from [8]:

$$\Delta G_{\text{ads}} = -RT \ln(55.5 \times K_{\text{ads}}), \quad (6)$$

where R is $8.314\,\mathrm{J \cdot mol^{-1}K^{-1}}$, T is absolute temperature (K), and 55.5 is the molar concentration of water.

The adsorption entropy (ΔS_{ads}) was determined using the thermodynamic relationship [13]:

$$\Delta G_{\text{ads}} = \Delta H_{\text{ads}} - T \times \Delta S_{\text{ads}}. \quad (7)$$

Kinetic studies were performed to assess activation parameters. The Arrhenius equation [13]:

$$\ln(CR) = \ln(A) - \frac{E_{\text{act}}}{RT}, \quad (8)$$

was used to determine activation energy (E_{act}), where CR is the corrosion rate, and the Eyring transition-state equation [14]:

$$\ln\left(\frac{CR}{T}\right) = \ln\left(\frac{R}{Nh}\right) + \frac{\Delta S_{\text{act}}}{R} - \frac{\Delta H_{\text{act}}}{RT}, \quad (9)$$

was applied to calculate activation enthalpy (ΔH_{act}) and activation entropy (ΔS_{act}), where h is the Planck's constant and N is the Avogadro's number.

Regression analysis of isotherm and kinetic plots enabled precise determination of K_{ads}, ΔG_{ads}, ΔH_{ads}, ΔS_{ads}, E_{act}, ΔH_{act}, ΔS_{act}, and ΔG_{act}, providing deep insight into the adsorption mechanism and confirming the efficiency of the inhibitor under acidic conditions.

2.4. Quantum chemical calculation

The inhibitory performance of the studied compound was further investigated through density functional theory DFT calculations to correlate electronic descriptors with adsorption behavior. Quantum chemical analyses were carried out using the B3LYP functional with the 6-31$G(d,p)$ basis set in the

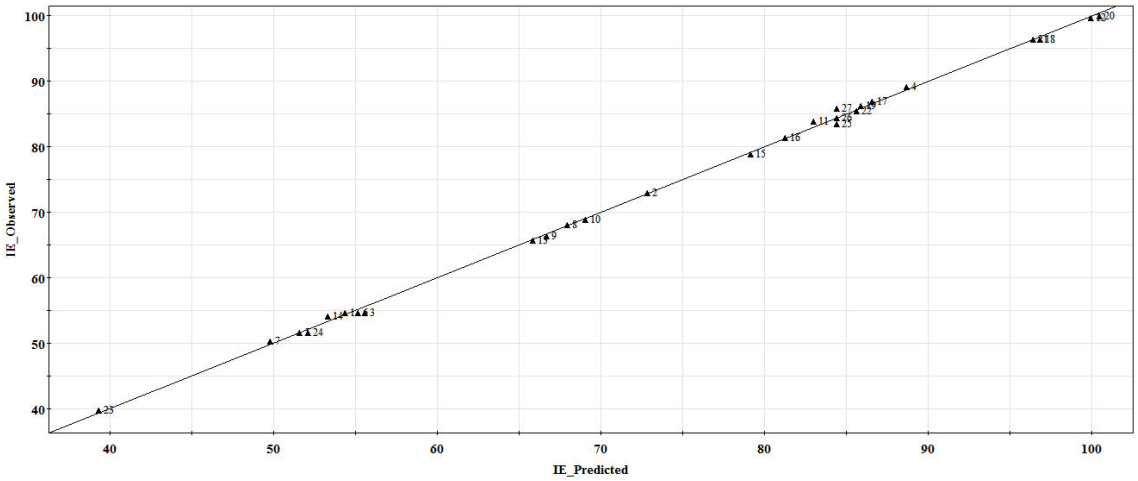


FIGURE 1. Parity plot showing the correlation between observed and predicted inhibition efficiency (IE%) for aopper in aulfuric acid medium.

Gaussian 09 software. Full geometry optimizations and conceptual DFT parameters were employed to evaluate molecular reactivity, stability, and adsorption propensity. These computational insights complement the experimental findings, providing a deeper understanding of the inhibition mechanism [15, 16].

3. Results and discussion

3.1. Design of experiments study

Response Surface Methodology RSM was applied to fit empirical models to the experimental data and systematically explore the effect of operating parameters on corrosion inhibition. A second-order polynomial model was selected to describe the system behavior and identify conditions that maximize performance. The independent variables considered were working temperature, immersion time, inhibitor concentration, and acid medium concentration, while the inhibition efficiency (IE%) served as the response parameter. A total of 27 experimental runs were conducted according to the designed matrix, allowing the estimation of both main and interaction effects. The results are presented in Table II, which compares the experimentally measured inhibition efficiencies with the values predicted by the developed model.

In the case of four independent variables, the system was described using the quadratic polynomial model given in Eq. (10):

$$\begin{aligned} \text{IE}\,(\%) = {} & 84.396 + 5.142\,x_1 + 7.278\,x_2 - 5.381\,x_3 \\ & + 6.390\,x_4 + 7.300\,x_1^2 + 8.773\,x_2^2 \\ & + 6.603\,x_3^2 - 38.703\,x_4^2 + 3.647\,x_1\,x_2 \\ & - 3.720\,x_1\,x_3 - 4.030\,x_1\,x_4 - 0.753\,x_2\,x_3 \\ & + 3.776\,x_2\,x_4 + 0.499\,x_3\,x_4, \end{aligned} \tag{10}$$

TABLE II. Comparison of experimental and eredicted inhibition efficiency (IE%) values with residuals and confidence intervals.

Run	IE (%)		Residual	Confidence
	Observed (Obs)	Predicted (Pred)	(Obs-Pred)	Interval (±)
1	54.55	54.362	0.188	1.435
2	72.92	72.845	0.075	1.435
3	54.58	55.574	-0.994	1.435
4	89.14	88.650	0.490	1.435
5	51.48	51.547	-0.067	1.435
6	54.55	55.159	-0.609	1.435
7	50.27	49.748	0.522	1.435
8	67.98	67.948	0.032	1.435
9	66.33	66.647	-0.317	1.435
10	68.82	69.017	-0.197	1.435
11	83.90	82.967	0.933	1.435
12	99.71	99.928	-0.218	1.435
13	65.67	65.835	-0.165	1.435
14	54.03	53.321	0.709	1.435
15	78.78	79.140	-0.360	1.435
16	81.35	81.214	0.136	1.435
17	86.82	86.558	0.262	1.258
18	96.42	96.837	-0.417	1.258
19	86.28	85.895	0.385	1.258
20	99.91	100.451	-0.541	1.258
21	96.42	96.379	0.041	1.258
22	85.42	85.617	-0.197	1.258
23	39.67	39.306	0.364	1.258
24	51.56	52.080	-0.520	1.258
25	83.42	84.394	-0.974	0.651
26	84.36	84.392	-0.032	0.651
27	85.87	84.397	1.473	0.651

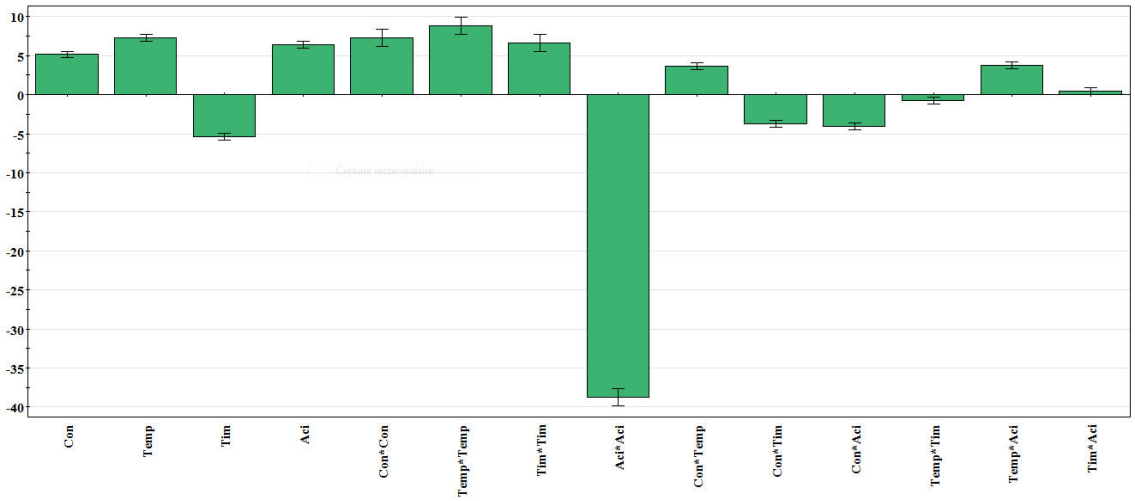


FIGURE 2. Standardized effect plot showing the relative influence and direction of main effects, quadratic terms, and two-factor interactions on the inhibition efficiency (IE%) of the organic inhibitor on copper in H_2SO_4 medium. Error bars represent confidence intervals.

TABLE III. Regression coefficients, standard errors, p-values, and confidence intervals for the model predicting inhibition efficiency (IE%).

Term Coded	Coded	Coefficient	Std. Error	p-value	Confidence Interval
Constant	-	84.396	0.299	2.63×10^{-24}	0.651
Con	X_1	+5.142	0.191	4.30×10^{-12}	0.417
Temp	X_2	+7.278	0.191	6.96×10^{-14}	0.417
Tim	X_3	-5.381	0.191	2.51×10^{-12}	0.417
Aci	X_4	+6.390	0.191	3.27×10^{-13}	0.417
Con ^{2}	X_1^2	+7.300	0.506	6.05×10^{-9}	1.102
Temp ^{2}	X_2^2	+8.773	0.506	7.34×10^{-10}	1.102
Tim ^{2}	X_3^2	+6.603	0.506	1.89×10^{-8}	1.102
Aci^2	X_4^2	-38.703	0.506	1.66×10^{-17}	1.102
Con × Temp	$X_1 \cdot X_2$	+3.647	0.203	4.81×10^{-10}	0.442
Con × Tim	$X_1 \cdot X_3$	-3.720	0.203	3.83×10^{-10}	0.442
Con × Aci	$X_1 \cdot X_4$	-4.030	0.203	1.51×10^{-10}	0.442
Temp × Tim	$X_2 \cdot X_3$	-0.753	0.203	2.96×10^{-3}	0.442
Temp × Aci	$X_2 \cdot X_4$	+3.776	0.203	3.22×10^{-10}	0.442
Tim × Aci	$X_3 \cdot X_4$	+0.499	0.203	3.01×10^{-2}	0.442

The close agreement between experimental and predicted IE% values, as shown in Table II, demonstrates the high predictive accuracy of the model, with all residuals falling well within the specified confidence intervals. Deviations across the dataset are minimal, with the highest residual (1.47%) remaining within statistical confidence bounds. Confidence intervals ranging from ± 0.65 to ± 1.43 confirm strong model precision. This narrow variation indicates high reproducibility and minimal experimental noise. The consistency of results across all runs demonstrates model stability. The close match between observed and estimated responses affirms the validity of the quadratic regression [17]. Residual patterns further validate that the model is well-calibrated. Such outcomes reinforce the credibility of the experimental protocol. The findings demonstrate that the model reliably captures the effects of tested variables. Overall, the model proves highly applicable for predicting corrosion inhibition efficiency under varying conditions. As visualized in Fig. 1, a parity plot comparing predicted and observed IE% values reveal that the data points closely align along the diagonal line of identity. This visual confirmation further validates the model's predictive power and affirms its suitability for simulating corrosion inhibition processes [18].

The model coefficients and associated statistics are presented in Table III, including standard errors, $p-$values, and confidence intervals. This model exhibits a strong fit to the experimental data, as supported by the very low standard errors and highly significant $p-$values ($p < 0.0001$) for most coefficients [19]. Notably, all linear terms inhibitor concentration, temperature, and acid concentration show positive coefficients, implying a direct enhancement of IE% with increasing values. In contrast, immersion time shows a nega-

tive impact, suggesting prolonged exposure may reduce the stability of the inhibitor film.

Quadratic terms reveal curvature in the response. While increasing X_1, X_2, and X_3 improves inhibition to a point, the negative coefficient of X_4^2 (-38.70) highlights a sharp decline in efficiency beyond an optimal acid concentration, likely due to aggressive solution breakdown of the protective layer. Interaction effects such as X_1X_2 ($+3.65$) and X_2X_4 ($+3.78$) suggest synergistic behavior between concentration and temperature, and temperature and acidity, respectively enhancing inhibition under combined optimal conditions. Conversely, X_1X_4 (-4.03) and X_1X_3 (-3.72) indicate potential destabilization when high inhibitor levels coincide with long immersion or strong acid environments. The model's intercept (84.396%) represents the average baseline efficiency, with optimal conditions yielding significantly higher values ($> 95\%$). The narrow confidence intervals (± 0.42 to ± 1.10) and small standard errors confirm the precision and reproducibility of the model (Table III). These statistical interpretations are visually reinforced in Fig. 2, which depicts the standardized effects of main factors, interaction terms, and quadratic contributions. The plot highlights the relative importance of each parameter, with the quadratic effect of acid concentration emerging as the most dominant. The inclusion of error bars illustrates the statistical significance of each term, further validating the model structure.

3.1.1. Interpretation of ANOVA and Model Significance

The analysis of variance (ANOVA), summarized in Table IV, confirms the robustness and statistical validity of the developed response surface model describing the inhibition efficiency (IE$\%$) of the organic inhibitor on copper in sulfuric acid solution. The model demonstrates excellent goodness-of-fit, with a coefficient of determination (R^2) of 0.999,

TABLE IV. Model adequacy parameters for inhibition efficiency model.

R^2 Adj.	R^2	Q^2	Cond. no.	Model Validity	Repro--ducibility	Conf Lev (%)
0.999	0.998	0.995	6.612	0.977	0.995	95

indicating that 99.9% of the total variation in the response is explained by the model. This is further supported by an adjusted R^2 of 0.998, reflecting stability even when accounting for the number of influencing variables. The predictive ability of the model is highlighted by a high cross-validated Q^2 value of 0.995, underscoring its strong generalization performance. In addition, a model validity score of 0.977 confirms the structural adequacy of the model and the absence of overfitting, while a reproducibility value of 0.995 attests to the consistency of results across replicate trials [20]. These key statistical indicators are graphically depicted in Fig. 3, which reinforces the model's reliability and predictive strength. A condition number of 6.612 confirms numerical stability and absence of multicollinearity.

Statistical significance is emphasized in Table V by a large F-value (867.23) and a highly significant $p-$value (< 0.0001), affirming that the examined factors namely, inhibitor concentration, temperature, acid molarity, and immersion duration exert a considerable effect on the corrosion inhibition process. In terms of explained variability, the total sum of squares ($\mathrm{SS} = 154,701$) includes all observed data variation, with $146,702$ associated with the constant term. The corrected SS (7999.77) isolates the contribution of experimental factors, and the regression model successfully accounts for nearly all of this value ($\mathrm{SS} = 7991.87$), leaving a minimal

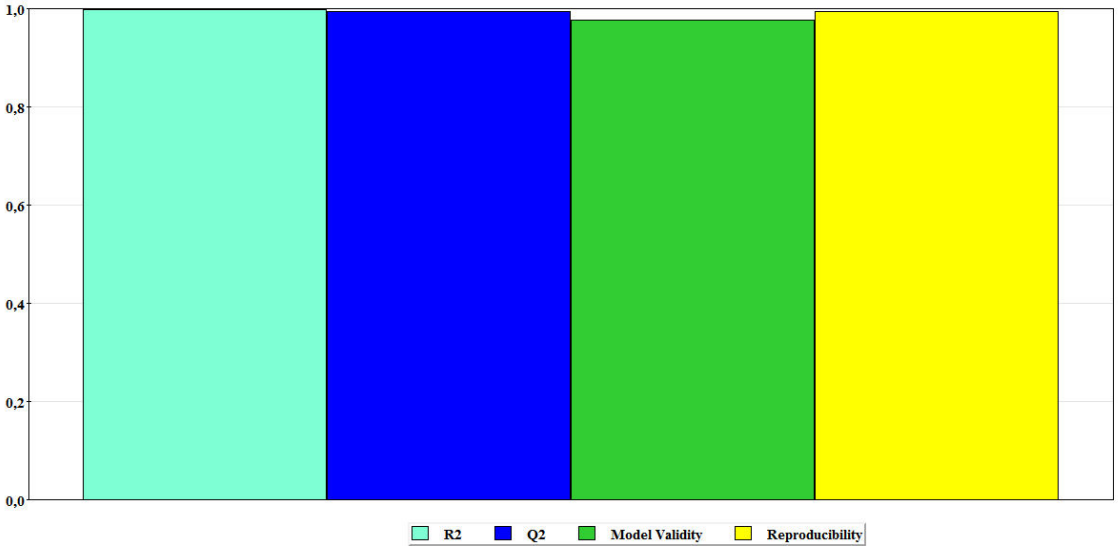


FIGURE 3. Statistical performance summary illustrating model goodness of fit (R^2), predictive ability (Q^2), model validity, and reproducibility.

TABLE V. Summary of ANOVA and model adequacy parameters for inhibition efficiency (IE%).

Source	DF	SS	MS	F	$p-$value	SD
Total	–	154701	5729.68	–	–	–
Constant	–	146702	146702	–	–	–
Total Corrected	26	7999.77	307.683	–	–	17.541
Regression	14	7991.87	570.848	867.229	0.000	23.892
Residual	12	7.89892	0.658	–	–	0.811
Lack of Fit	10	4.85116	0.485	0.3183	0.913	0.696
Pure Error	2	3.04776	1.524	–	–	1.234

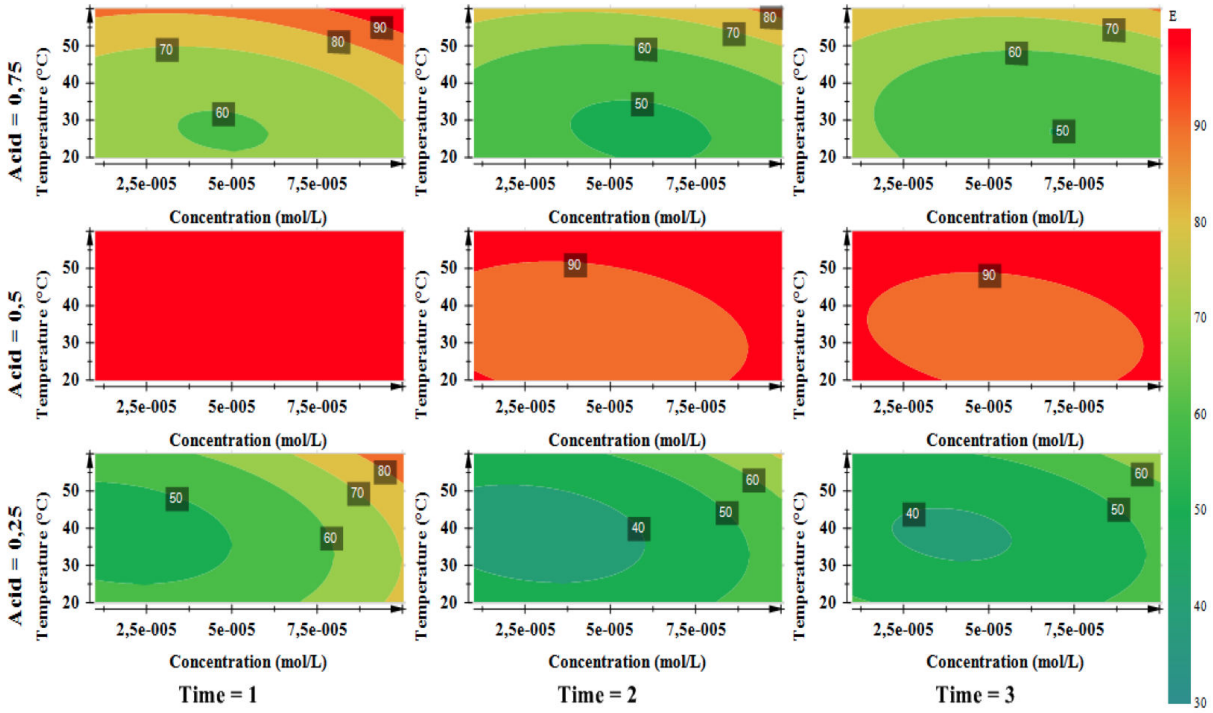


FIGURE 4. Four-dimensional contour plots illustrating the combined effects of acid and inhibitor concentration, temperature, and immersion time on the inhibition efficiency (IE%) of an organic compound against copper corrosion in sulfuric acid media.

residual SS of 7.90. The lack-of-fit test yields a non-significant $p-$value of 0.913, confirming that the model predictions closely align with experimental observations and that remaining variation is due to random experimental noise. A low residual mean square (0.658) and standard deviation (RSD $= 0.8113$) further indicate high model precision. The pure error SD (1.23), derived from replicates, is within acceptable limits, and the lack-of-fit SD (0.70) demonstrates consistent model performance across the design space.

Figure 4 presents four-dimensional contour plots illustrating the influence of four experimental factors on a single response variable: the corrosion inhibition efficiency (IE%) of an organic compound on copper in a sulfuric acid medium. Each subplot corresponds to a fixed immersion time (1, 2, or 3 hours), with inhibitor concentration and temperature plotted along the $x-$ and $y-$axes, respectively. Acid concentration varies across the three rows (0.25, 0.5, and 0.75 M). The color gradient represents the magnitude of inhibition efficiency, with red areas indicating higher IE% values. A pronounced enhancement in inhibition efficiency is observed at higher acid concentrations (0.5 and 0.75 M), particularly when combined with elevated inhibitor doses and temperatures. These regions exhibit inhibition efficiencies exceeding 90%, underscoring the compound's superior performance in more corrosive environments likely due to accelerated adsorption kinetics facilitated by increased electrochemical activity. This finding highlights the inhibitor's robustness under aggressive acidic conditions. In contrast, at lower acid concentrations (0.25 M), efficiency is generally reduced, with IE values concentrated in the $40-70\%$ range. The optimal per-

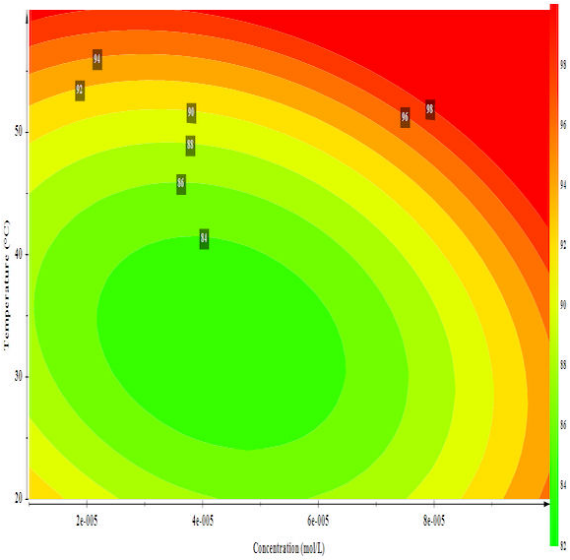


FIGURE 5. Contour plot analysis of corrosion inhibition efficiency with varying concentration and temperature.

formance at $0.25\,\mathrm{M}$ occurs only at elevated concentrations and temperatures, showing the critical need for proper dosage under milder acidic conditions. The immersion time also plays a key role. At 1 hour, performance is generally better across all conditions. However, at 2 and 3 hours, a decline in IE is observed in most subplots, possibly due to inhibitor desorption or degradation over time. Overall, these results confirm that maximum corrosion inhibition is achieved through a synergistic combination of high acid concentration, optimized inhibitor dose, moderate to high temperature, and short exposure times.

Figure 5 complements this with a $2D$ contour map that offers precise visual gradients. Efficiency is lowest at the core of the plot (green zone), corresponding to low concentrations and temperatures. Moving radially outward, the contour lines shift through yellow, orange, and finally red, signifying steady improvement in IE$\%$. The highest efficiency (98%) is achieved near $8 \times 10^{-5}\ \mathrm{L}^{-1}\ \mathrm{mol}$ and around $60\,^{\circ}\mathrm{C}$. Figure 6

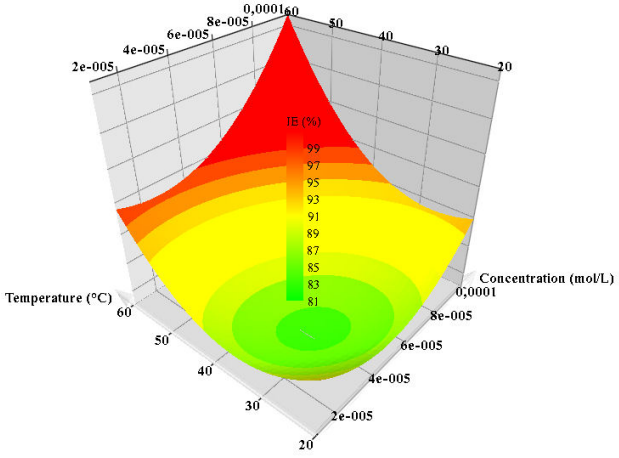


FIGURE 6. Response surface analysis of corrosion inhibition efficiency with varying concentration and temperature.

illustrates a $3D$ response surface demonstrating the relationship between inhibition efficiency (IE$\%$), organic inhibitor concentration, and temperature. Conducted at a fixed immersion time of 2 hours in 0.5 M H_2SO_4, the graph reveals a parabolic rise in IE$\%$ with increasing temperature and inhibitor levels. The elevated region of the surface identifies optimal conditions where inhibition exceeds 96%, reflecting a strong synergistic interaction. The combined surface and contour plots emphasize the significant role of temperature and inhibitor concentration in optimizing corrosion resistance. The model's consistency and predictive accuracy are confirmed by the smooth response trends. This visual analysis effectively supports parameter optimization for improved inhibitor performance in acidic media.

3.1.2. Main effects

Figure 7 illustrates the individual impact of three key parameters concentration, temperature, and immersion time on the inhibition efficiency (IE$\%$) of the tested organic inhibitor. Each plot presents the mean IE$\%$ corresponding to a specific level of the studied variable, while the other conditions were held constant. The first plot reveals a slight initial decline in IE$\%$ as inhibitor concentration increases up to approximately $5.5 \times 10^{-5}\ \mathrm{mol \cdot L^{-1}}$, reaching a minimum of around 84%. Beyond this threshold, a marked improvement in efficiency is observed, surpassing 96% at the highest concentration ($1 \times 10^{-4}\,\mathrm{mol \cdot L^{-1}}$). This behavior suggests the existence of a critical surface coverage level, above which the formation of a compact and stable protective film becomes increasingly effective. The second plot demonstrates a nonlinear relationship between temperature and inhibition performance. A minor decrease in IE$\%$ is noted up to $40\,^{\circ}\mathrm{C}$, followed by a pronounced increase, with efficiency peaking near $60\,^{\circ}\mathrm{C}$. This temperature-dependent trend is typical of adsorption processes with a chemisorptive character, where increased thermal energy enhances molecular interaction with the metal surface and promotes inhibitor film stability. The third plot indicates a decline in inhibition efficiency between 1 and 2 hours of immersion, likely due to partial desorption or temporary instability of the adsorbed film. However, efficiency rises again at 3 hours, which may be attributed to readsorption or structural reorganization of the inhibitor layer. These variations underscore the dynamic equilibrium of the adsorption process and highlight the importance of identifying an optimal immersion time for sustained corrosion protection [21].

3.2. Adsorption Considerations and Activation Energy Calculations

3.2.1. Activation parameters of corrosion process

Determination of activation parameters offers critical insights into how temperature influences corrosion dynamics and the development of protective surface layers. In this work, the activation energy, activation enthalpy, activation entropy, and

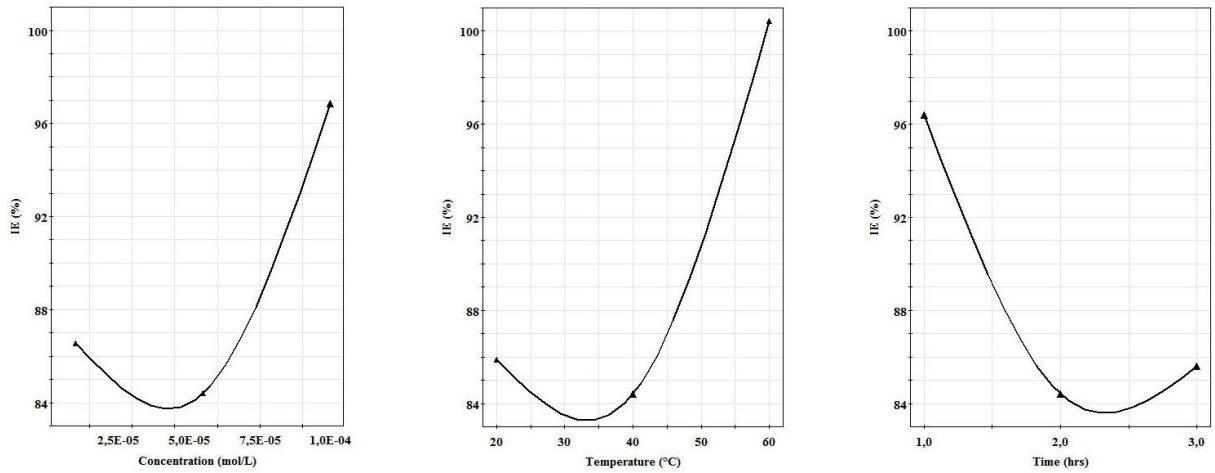


FIGURE 7. Effect of inhibitor concentration, temperature, and immersion time on the corrosion inhibition efficiency of an organic compound for copper in 0.5 M H_2SO_4, with fixed experimental conditions ($C = 5.5 \times 10^{-5}\,\mathrm{mol \cdot L^{-1}}$, $T = 40\,^{\circ}\mathrm{C}$, and immersion time $= 2\mathrm{h}$) for non-varied parameters.

activation Gibbs free energy were evaluated for copper corrosion in 0.5 M H_2SO_4, both in the absence and presence of the organic inhibitor. These parameters provide a detailed kinetic and thermodynamic perspective on the inhibition mechanism, thereby enhancing the understanding of corrosion control strategies.

The blank sample, without inhibitor, exhibits the lowest activation energy ($7.36\,\mathrm{kJ \cdot mol^{-1}}$), indicating minimal resistance to corrosion. Upon the introduction of the organic inhibitor, E_{act} values rise significantly, reaching up to $40.38\,\mathrm{kJmol^{-1}}$ at $1.0 \times 10^{-4}\,\mathrm{mol \cdot L^{-1}}$. This increase reflects a heightened energy barrier to copper dissolution, attributed to the inhibitor's protective action, and suggests a transition from an uninhibited to a physisorption-dominated mechanism [22].

All ΔH_{act} values are positive, confirming that the corrosion process is endothermic requiring energy input for metal dissolution [23]. The close correspondence between E_{act} and ΔH_{act} (with $E_{\text{act}} - \Delta H_{\text{act}} \approx RT$) validates the kinetic consistency and supports the assumption of a unimolecular reaction pathway, often associated with hydrogen evolution as the rate-determining step [24]. Meanwhile, the negative entropy of activation (ΔS_{act}) values ranging from -302.53 to $-214.65\,\mathrm{J \cdot mol^{-1} \cdot K^{-1}}$ reflect a decrease in disorder during the formation of the activated complex, indicative of an associative mechanism. This implies a more ordered transition state, possibly due to strong inhibitor-metal surface interactions.

The activation free energy (ΔG_{act}), was consistently positive and increased with temperature, confirming the non-spontaneous nature of the rate-determining step. This rise indicates that additional thermal energy is required to overcome the activation barrier, reflecting a temperature-dependent process. Furthermore, higher inhibitor concentrations yielded elevated ΔG_{act} values, attributed to the formation of a stable protective adsorption layer [25]. These results demonstrate that the organic inhibitor effectively modifies the activation pathway, thereby suppressing copper dissolution.

3.2.2. Adsorption Isotherm and Thermodynamic Parameters

Adsorption isotherms are essential tools for understanding the nature and mechanism of organic inhibitor interaction with metal surface. Determining the most suitable isotherm model provides valuable insights into the adsorption behavior, surface coverage, and molecular orientation of the inhibitor. In this study, several adsorption isotherm models namely Langmuir, Temkin, Freundlich, Flory-Huggins, El-Awady, and Frumkin were evaluated to analyze the adsorption of the tested inhibitor onto copper surfaces in 0.5 M H_2SO_4 across a temperature range of 293 to 333 K.

The correlation coefficients (R^2) derived from weight loss measurements (Table VI) demonstrate that the Langmuir isotherm consistently exhibits the highest R^2 values at all temperatures, suggesting that the adsorption process primarily follows Langmuir behavior. This implies monolayer adsorption with no interaction between adsorbed species [26]. Although other models such as Temkin, Freundlich, and

TABLE VI. Adsorption values calculated from the Langmuir isotherm.

T	R^2	K_{ads}	ΔH_{ads}	ΔS_{ads}	ΔG_{ads}
K		$\mathrm{Lmol^{-1}}$	$\mathrm{kJmol^{-1}}$	$\mathrm{Jmol^{-1}K^{-1}}$	$\mathrm{kJmol^{-1}}$
293	0.998	2.10×10^5		19.59	-39.64
303	0.996	1.38×10^5		19.94	-39.94
313	0.989	0.88×10^5	-33.99	19.78	-40.09
323	0.975	0.57×10^5		19.45	-40.18
333	0.965	0.40×10^5		19.77	-40.48

Frumkin also showed moderate to good correlations at specific temperatures, their lower R^2 values compared to Langmuir support the dominance of Langmuir-type adsorption under the studied conditions.

The K_{ads} values were found to decrease with increasing temperature (Table VI), suggesting that adsorption becomes less favorable at higher temperatures [26].

The negative values of ΔG_{ads} (ranging from -39.64 to $-40.48\,\text{kJmol}^{-1}$) indicate a spontaneous and thermodynamically favorable interaction between the inhibitor molecules and the copper surface. Since these values fall between -20 and -40 kJmol^{-1}, the adsorption mechanism likely involves mixed-mode adsorption, combining physisorption and chemisorption [24]. The adsorption process in this study is characterized by an exothermic enthalpy of adsorption (ΔH_{ads}) of -33.99 kJmol^{-1}, indicative of physisorption, as it falls below the typical threshold of 40 kJmol^{-1} associated with weak van der Waals interactions. In contrast, chemisorption generally involves higher enthalpy values near 100 kJmol^{-1} due to stronger chemical bonds [27]. Furthermore, the positive values of the entropy change (ΔS_{ads}) reflect an increase in disorder at the metal/solution interface. This rise in entropy is often attributed to the displacement of water molecules by inhibitor molecules during adsorption, which increases randomness in the system and contributes to spontaneity [28].

3.3. Quantum chemical calculation

Theoretical insights derived from quantum chemical descriptors underscore the promising inhibitory performance of the studied compound on copper in acidic media. The descriptor calculations shown in Table VII are based on theoretical formulations previously established in the quantum chemical literature [29, 30]. The frontier orbital energies, EHOMO ($-6.402\,\text{eV}$) and ELUMO ($-3.318\,\text{eV}$), indicate dual electron-donating and accepting behavior. As shown in Fig. 8, the HOMO is mainly localized on heteroatoms (N, O, S) and $\pi-$systems, to the vacant copper $3d$ orbitals. Conversely, in Fig. 9 the LUMO enables electron acceptance from the metal via $\pi-$back-donation. This bidirectional charge transfer strengthens donor-acceptor interactions at the interface and contributes to the formation of a stable chemisorbed protective layer. Together, Figs. 8 and 9 integrate quantum chemical and mechanistic perspectives, providing compelling evidence that electrostatic attraction, covalent coordination, and π-metal interactions act simultaneously to suppress both anodic dissolution and cathodic processes in strongly acidic environments [32].

The moderate HOMO-LUMO energy gap ($3.084\,\text{eV}$) highlights a balance between electronic reactivity and molecular stability, enabling efficient surface interactions without compromising durability [31]. The inhibitor's electronega-

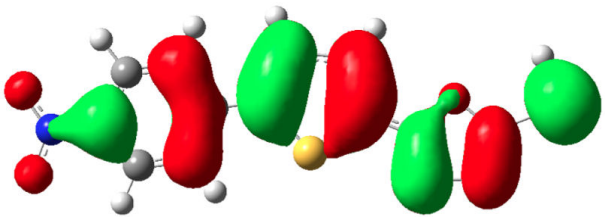


FIGURE 8. Frontier molecular orbitals (HOMO) of 5-(5-(4-nitrophenyl)thiophen2-yl)-1,3,4-oxadiazole-2(3H)-thione (3) computed at the DFT/B3LYP/6-311++(d,p) level of theory.

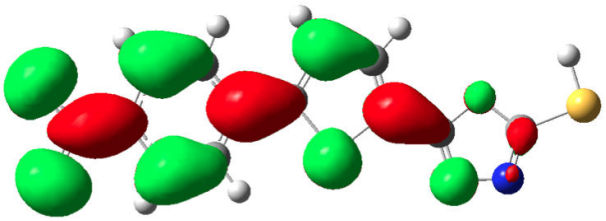


FIGURE 9. Frontier molecular orbitals (LUMO) of 5-(5-(4-nitrophenyl)thiophen2-yl)-1,3,4-oxadiazole-2(3H)-thione (3) computed at the DFT/B3LYP/6-311++(d,p) level of theory.

TABLE VII. Quantum chemical descriptors of 5-(5-(4-nitrophenyl)thiophen-2-yl)-1,3,4-oxadiazole-2(3H)-thione 3 and their theoretical significance for corrosion inhibition on copper in acidic media.

Parameter	Equation / Formula	Value
$EHOMO$	$-IP$	-6.402 eV
$ELUMO$	$-EA$	-3.318 eV
Energy Gap (E_{gap})	$E_{\text{gap}} = E_{\text{LUMO}} - E_{\text{HOMO}}$	3.084 eV
Electronegativity (χ)	$\chi = (IP + EA)/2$	4.860 eV
Hardness (η)	$\eta = (IP - EA)/2$	1.542 eV
Number of electrons transferred (ΔN)	$\Delta N = (\chi Cu - \chi_{\text{inh}})/[2(\eta Cu + \eta_{\text{inh}})]$	-0.139
Electrophilicity index (ω)	$\omega = \chi^2/(2\eta)$	7.659 eV
Back-donation energy ($\Delta E_{\text{back-donation}}$)	$\Delta E = -\eta/4$	-0.385 eV
Softness (S)	$S = 1/(2\eta)$	$0.324\,\text{eV}^{-1}$
$Q_{\max}$	$Q_{\max} = -\chi/\eta$	-3.152

tivity (4.860 eV), being close to that of copper, facilitates charge-transfer equilibrium and promotes strong adsorption [32]. Its chemical hardness (1.542 eV) reflects resistance to electronic deformation, while the corresponding softness ($0.324\,\mathrm{eV}^{-1}$) indicates adequate polarizability at the metal-solution interface [33]. The sign of ΔN determines the direction of electron transfer at the inhibitor-metal interface according to the Pearson electronegativity formalism proposed by Lukovits [34]. Within the convention employed in this work, a positive ΔN value indicates electron donation from the inhibitor molecule toward the metal surface, whereas a negative ΔN value reflects a tendency toward electron back donation from the metal to the inhibitor [35]. In the present case, the calculated value ($\Delta N = -0.139$, using $\chi_{\mathrm{Cu}} = 4.43\,\mathrm{eV}$ and $\eta_{\mathrm{Cu}} = 0\,\mathrm{eV}$) suggests that the inhibitor behaves predominantly as an electron acceptor relative to copper, which may contribute to stabilizing the adsorbed protective layer through metal to inhibitor back donation interactions [36]. The electrophilicity index (7.659 eV) and maximum charge acceptance ($Q_{\max} = -3.152$) further illustrate the molecule's ability to accommodate and stabilize charge density, a key factor for persistent adsorption [37]. The negative back-donation energy ($-0.385\,\mathrm{eV}$) indicates that back-donation from copper orbitals is energetically favorable, reinforcing the inhibitor-substrate interaction [33]. Finally, the electrodonating ($W^- = 3.322$) and electroaccepting ($W^+ = 0.892$) powers emphasize a predominantly nucleophilic character, consistent with efficient electron donation to vacant copper orbitals [38].

3.4. Proposed mechanism of corrosion inhibition

In 0.5 M H_2SO_4, copper undergoes active dissolution rather than forming a protective passive layer, progressing mainly through sequential oxidation from Cu^0 to Cu^{2+} with Cu^+ as a transient intermediate [1]. Under aerated conditions, oxygen reduction dominates the cathodic pathway, whereas hydrogen evolution becomes more significant in deaerated environments. Sulfate anions strongly adsorb on the copper surface, imparting a negative charge that promotes electrostatic attraction with protonated NPT-OxT molecules [39]. This interaction triggers an initial physisorption stage through the displacement of interfacial water molecules:

$$\mathrm{Inh}_{(\mathrm{sol})} + x\,\mathrm{H_2O}_{(\mathrm{ads})} \underset{\leftarrow}{\rightarrow} \mathrm{Inh}_{(\mathrm{ads})} + x\,\mathrm{H_2O}_{(\mathrm{sol})}.$$

As shown in Fig. 10, molecular electrostatic potential MEP mapping identifies electron-rich domains around heteroatoms (N, O, S) and within the $\pi-$conjugated framework as the most favorable sites for interaction with copper atoms. These regions orient toward the metal, facilitating donor-acceptor interactions. This stage is followed by chemisorption, where lone pairs on heteroatoms coordinate with vacant Cu 3d orbitals, forming stable $\mathrm{Cu-N}$ and $\mathrm{Cu-S}$ bonds that enhance film compactness and persistence. In parallel, the extended $\pi-$system of the thiophene and nitrophenyl groups participates in $\pi-$d interactions and back-donation from

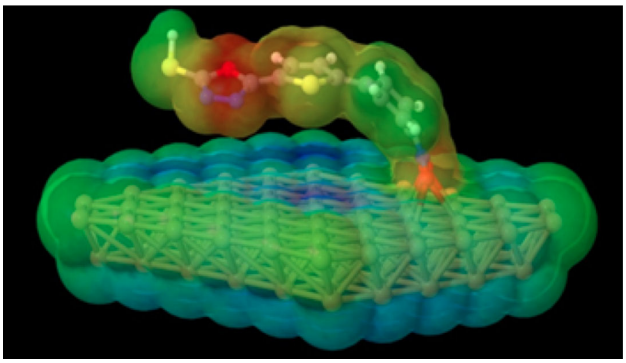


FIGURE 10. Adsorption of 5-(5-(4-nitrophenyl)thiophen-2-yl)1,3,4-oxadiazole-2(3H)-thione on copper surface in sulfuric acidic medium: molecular electrostatic potential representation.

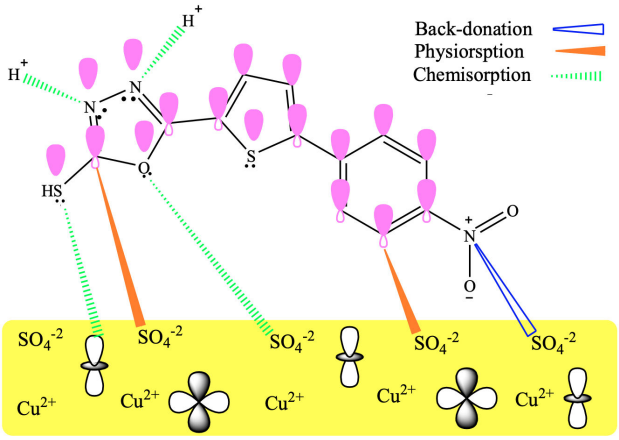


FIGURE 11. Adsorption model proposed for 5-(5-(4-nitrophenyl) thiophen-2-yl)-1,3,4-oxadiazole-2(3H)-thione on copper in sulfuric acidic solution.

filled Cu d-orbitals into the inhibitor's π^* orbitals, reinforcing the organic layer. Complementing these interactions, $\mathrm{Cu}(I)-$inhibitor complex formation may occur either directly at the interface or in solution:

$$\mathrm{Cu} + \mathrm{Inh} \rightarrow \mathrm{Cu-Inh}_{(\mathrm{ads})},$$

$$\mathrm{Cu}^+_{(\mathrm{aq})} + \mathrm{Inh}_{(\mathrm{aq})} \rightarrow \mathrm{Cu}(I)\,\mathrm{Inh}_{(s)} + \mathrm{H}^+_{(\mathrm{aq})}.$$

The schematic overview in Fig. 11 summarizes this synergistic inhibition pathway. It illustrates how physisorption initiates surface coverage, while chemisorption, π-back-donation, and $\mathrm{Cu}(I)-$inhibitor complexation stabilize a dense and insoluble protective layer [40].

3.5. Surface morphology characterization and Energy dispersive X ray

The SEM micrographs presented in Fig. 12, 13 and 14 visually demonstrate the influence of 5-(5-(4-nitrophenyl)thiophen-2-yl)-1,3,4-oxadiazole-2(3H)-thione on the surface morphology of copper exposed to sulfuric acid at 298 K for 90 min. The polished copper surface (Fig. 12)

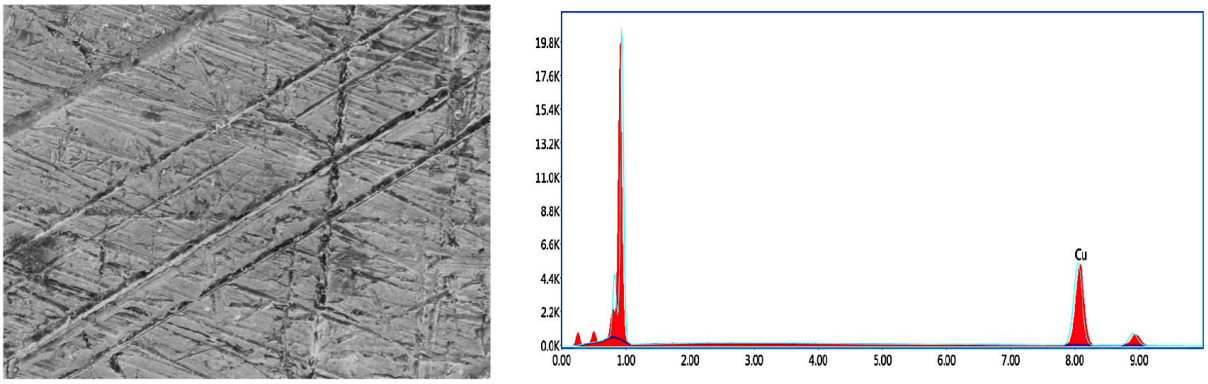


FIGURE 12. SEM micrographs and corresponding EDX spectra of copper surfaces: polished metal.

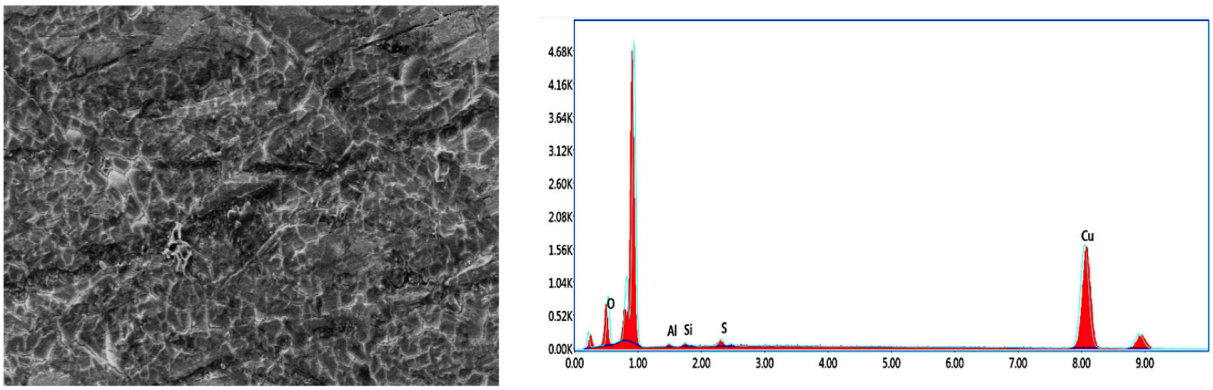


FIGURE 13. SEM micrographs and corresponding EDX spectra of copper surfaces: after 90 min immersion in $0.5\,\mathrm{M}\,H_2SO_4$.

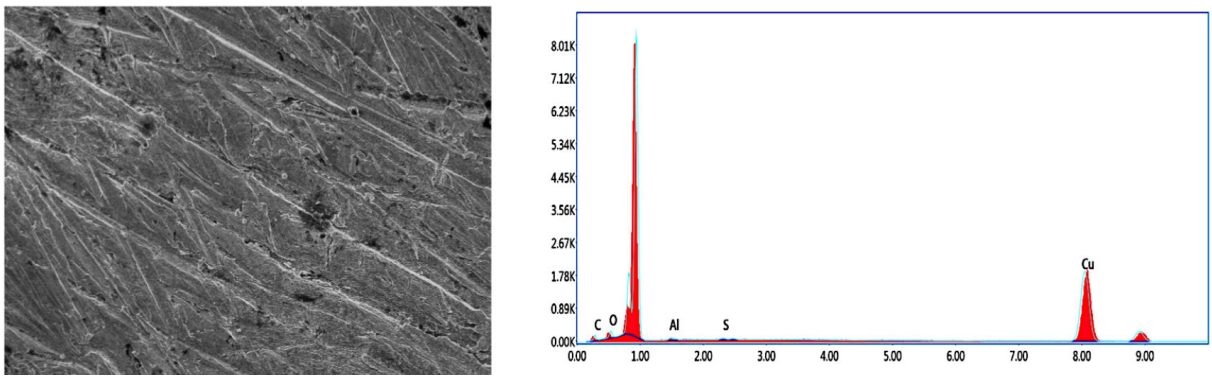


FIGURE 14. SEM micrographs and corresponding EDX spectra of copper surfaces: after immersion in 0.5 M H_2SO_4 containing $1 \times 10^{-4}\,\mathrm{mol\,L^{-1}}$ of 5-(5-(4-nitrophenyl)thiophen-2-yl)-1,3,4-oxadiazole-2(3H)-thione inhibitor.

displays a uniform texture with fine polishing marks, serving as a reference for comparison. After immersion in 0.5 M H_2SO_4 without inhibitor (Fig. 13), the surface becomes severely damaged, exhibiting rough morphology and dense corrosion products, which confirm the aggressive dissolution of copper in acidic media [18]. In contrast, the specimen immersed in the inhibited solution (Fig. 14) reveals a markedly smoother and more compact surface, indicating a significant reduction in corrosion activity.

The EDX spectra provide elemental composition data that support the morphological observations. For the polished copper surface (Fig. 12), the spectrum is dominated by a strong copper peak, indicating a clean, uncontaminated metal surface. After immersion in 0.5 M H_2SO_4 without inhibitor (Fig. 13), the EDX spectrum shows a significant decrease in the copper signal and the appearance of oxygen and sulfur peaks, suggesting the formation of copper sulfate or oxide corrosion products. In the presence of the inhibitor (Fig. 14), the copper peak remains prominent, while the oxygen and sulfur signals are considerably reduced. This indicates that the inhibitor effectively limits the interaction between the copper surface and the corrosive ions, thereby re-

ducing the formation of corrosion products and preserving the metallic character of the surface. This improvement is attributed to the adsorption of NPT-OxT molecules onto the copper surface, forming a coherent protective layer that restricts the access of H^+ and SO_4^{2-} ions to the metal. Hence, the SEM and EDX observations corroborate the electrochemical results, confirming that NPT-OxT acts as an efficient surface-active inhibitor for copper in sulfuric acid solution. Hence, the SEM observations corroborate the electrochemical results, confirming that NPT-OxT acts as an efficient surface-active inhibitor for copper in sulfuric acid solution.

4. Conclusion

This work identifies 5-(5-(4-nitrophenyl)thiophen-2-yl)-1,3,4-oxadiazole-2(3H)-thione (NPT-OxT) as an exceptionally efficient corrosion inhibitor for copper in $0.5\,\mathrm{M}\,H_2SO_4$, reaching 97% inhibition efficiency under conditions optimized by Response Surface Methodology RSM. Beyond conventional empirical reporting, this study combines statistical modeling and quantum chemical analysis to unravel the inhibition mechanism from both macroscopic and molecular perspectives. The RSM model ($R^2 = 0.999$) revealed a synergistic interaction among inhibitor concentration, temperature, and medium acidity, providing a precise predictive tool for corrosion control.

Thermodynamic and kinetic analyses demonstrated that adsorption occurs spontaneously ($\Delta G^{\circ}_{ads} \approx -40\,\mathrm{kJmol^{-1}}$) according to the Langmuir isotherm, with a mixed physisorption-chemisorption mode. The marked rise in activation energy (from 7.36 to $40.38\,\mathrm{kJmol^{-1}}$) confirms the formation of a stable, protective interfacial film. DFT calculations further validated these findings at the atomic level: a moderate HOMO-LUMO gap ($3.084\,\mathrm{eV}$) and a negative ΔN (-0.139) highlight efficient charge transfer through electron donation and back-donation processes. Complementary SEM analyses visually confirmed these results, revealing severe surface degradation on the uninhibited copper and a remarkably smooth, compact morphology in the presence of NPT-OxT. This was quantitatively supported by EDX analysis, which showed a strong, preserved copper signal and minimal oxygen and sulfur content on the inhibited surface. The observed microstructural refinement and absence of corrosion products attest to the formation of a dense, adherent protective layer on the copper surface. The proposed mechanism involves initial electrostatic attraction of the inhibitor to the metal surface, followed by coordination through heteroatoms and π-back-donation, producing a compact, adherent, and insoluble barrier layer.

Acknowledgements

The authors thank the Galicia Supercomputing Center (CESGA, Spain) for providing its computing resources, and the Center for Nanotechnology & Biomaterials Application and Research (NBUAM) at Marmara University (Turkey) for performing the SEM and EDX analyses.

1. K. Yoo *et al*., Improvement of copper metal leaching in sulfuric acid solution by simultaneous use of oxygen and cupric ions, *Metals* **10** (2020) 721, 10.3390/met10060721
2. W. Malec *et al*., Comparative studies of the properties of copper components: conventional vs. additive manufacturing technologies, *Metals* **14** (2024) 975, 10.3390/met14090975
3. T. Attar and A. Benchadli, Studying the effectiveness of an expired betamethasone drug in sulfuric acid solutions to examine the corrosive behavior of copper using weight loss and experimental design, *J. Turk. Chem. Soc. Sect. A* **11** (2024) 291, 10.18596/jotcsa.1353785
4. N. Guo *et al*., Corrosion mechanism of copper in seawater containing the bacterial pyomelanin with redox activity, *Corrosion Science* **204** (2022) 110407, 10.1016/j.corsci.2022.110407
5. N. Chabane *et al*., Green inhibition of copper corrosion by Ammoides verticillata oil in 1 M nitric acid: weight loss and Raman spectroscopic mapping studies, *Rev. Roum. Chim.* **68** (2023) 371, 10.33224/rrch.2023.68.7-8.06
6. A. H. Moustafa *et al*., An exploratory experimental analysis backed by quantum mechanical modeling, spectroscopic, and surface study for c-steel surface in the presence of hydrazone-based Schiff bases to fix corrosion defects in acidic media, *ACS Omega* **9** (2024) 16469, 10.1021/acsomega.4c00199
7. K. Shwetha, B. Praveen, and B. K. Devendra, A review on corrosion inhibitors: types, mechanisms, electrochemical analysis, corrosion rate and efficiency of corrosion inhibitors on mild steel in an acidic environment, *Results Surf. Interfaces* **16** (2024) 100258, 10.1016/j.rsurfi.2024.100258
8. Y. Datoussaid *et al*., Experimental and theoretical studies of aminothiophene derivatives inhibitors on carbon steel corrosion in perchloric acid medium, *Rev. Roum. Chim.* **69** (2024) 139, 10.33224/rrch.2024.69.3-4.04
9. A. Khormali and S. Ahmadi, Experimental and modeling analysis on the performance of 2-mercaptobenzimidazole corrosion inhibitor in hydrochloric acid solution during acidizing in the petroleum industry, *J. Pet. Explor. Prod. Technol.* **13** (2023) 2217, 10.1007/s13202-023-01675-6
10. S. Hadisaputra *et al*., Theoretical study of the substituent effect on corrosion inhibition performance of benzimidazole and its derivatives, *Int. J. Corros. Scale Inhib.* **8** (2019) 673, 10.17675/2305-6894-2019-8-3-15
11. P. P. Kumari and M. Lavanya, Optimization strategies for corrosion management in industries with artificial neural network and response surface technology: a comprehensive review, *J. Bio- Tribo-Corros.* **10** (2024) 59, 10.1007/s40735-024-00863-z

12. S. Ahmadi and A. Khormali, Optimization of the corrosion inhibition performance of 2-mercaptobenzothiazole for carbon steel in HCl media using response surface methodology, *Fuel* **357** (2024) 129783, 10.1016/j.fuel.2023.129783
13. T. Attar *et al*., Enhancing corrosion resistance of carbon steel in sulfuric acid using β-cyclodextrin as an inhibition, *Fr.-Ukr. J. Chem.* **11** (2023) 8, 10.17721/fujcV11I2P8-18
14. T. Attar, A. Benchadli, and E. Choukchou-Braham, Inhibition of corrosion of copper by polyvinylpyrrolidone-iodine in sulfuric acid medium, *Alg. J. Mat. Chem.* **5** (2022) 1, 10.57277/AJMC.2022.0501
15. N. Timoudan *et al*., Corrosion inhibition performance of benzimidazole derivatives for protection of carbon steel in hydrochloric acid solution, *RSC Adv.* **14** (2024) 30295, 10.1039/D4RA05070C
16. N. Betti *et al*., Corrosion inhibition properties of Schiff base derivative against mild steel in HCl environment complemented with DFT investigations, *Sci. Rep.* **13** (2023) 8979, 10.1038/s41598-023-36064-w
17. D. Prabhu, P. R. Prabhu, and P. Rao, Thermodynamics, adsorption, and response surface methodology investigation of the corrosion inhibition of aluminum by Terminalia chebula extract in H3PO4, *Chem. Pap.* **75** (2021) 653, 10.1007/s11696-020-01318-8
18. M. Fellahi, Y. Datoussaid, and M. E. A. Dib, Experimental design and statistical modeling for evaluating inhibition efficiency of Daucus crinitus essential oil in corrosion processes, *S. Afr. J. Chem.* **79** (2025) 117, 10.17159/0379-4350/2025/v79a12
19. M. Driouch *et al*., Development and validation of QSPR models for corrosion inhibition of carbon steel by some pyridazine derivatives in acidic medium, *Heliyon* **6** (2020) e05067, 10.1016/j.heliyon.2020.e05067
20. A. Benchadli *et al*., Optimization of inhibition efficiencies process of polyvinylpyrrolidone using response surface methodology, *Rev. Mex. Fís.* **68** (2022) 041003, 10.31349/RevMexFis.68.041003
21. M. A. M. Alwi *et al*., Gravimetric and electrochemical statistical optimizations for improving copper corrosion resistance in hydrochloric acid using thiosemicarbazone-linked 3-acetylpyridine, *RSC Adv.* **12** (2022) 27793, 10.1039/D2RA05192C
22. G. H. Ibrahim *et al*., Studies on the impact for pyrimidine compounds upon aluminum corrosion protection in acidic conditions, both experimentally and theoretically, *Egypt. J. Chem.* **66** (2023) 367, 10.21608/ejchem.2023.190675.7559
23. B.-L. Lin *et al*., Adsorption and corrosion of renewable inhibitor of pomelo peel extract for mild steel in phosphoric acid solution, *Arab. J. Chem.* **14** (2021) 103114, 10.1016/j.arabjc.2021.103114
24. T. Attar *et al*., Iodine–β-cyclodextrin: an effective corrosion inhibitor for carbon steel in sulfuric acid solution, *J. Turk. Chem. Soc. Sect. A* **11** (2024) 161, 10.18596/jotcsa.1346065
25. T. Attar *et al*., Experimental and theoretical studies of polyvinylpyrrolidone-iodine on carbon steel corrosion in 1 M hydrochloric solution, *Rev. Roum. Chim.* **66** (2021) 761, 10.33224/rrch.2021.66.8-9.10
26. A. A. Adamu, O. R. A. Iyun, and J. D. Habila, Adsorption and thermodynamic studies of the corrosion inhibition effect of Desmodium adscendens extract on carbon steel in 2 M HCl, *BMC Chem.* **19** (2025) 163, 10.1186/s13065-025-01541-y
27. M. M. Solomon *et al*., Corrosion inhibition of N80 steel in simulated acidizing environment, *J. Mol. Liq.* **273** (2019) 476, 10.1016/j.molliq.2018.10.032
28. N. Gupta *et al*., Thermodynamic study of green corrosion inhibitor on mild steel with aqueous extract of Ziziphus jujuba, *Chem. Sci. Rev. Lett.* **9** (2020) 6, 10.37273/chesci.CS205204097
29. R. Solmaz *et al*., Comprehensive experimental and theoretical study on adsorption and corrosion inhibition efficiency of pyronin B, *J. Phys. Chem. C* **128** (2024) 21809, 10.1021/acs.jpcc.4c06003
30. T. Attar *et al*., Corrosion inhibition efficiency of neutral red dye for carbon steel in perchloric acidic media, *Chem. Chem. Technol.* **16** (2022) 440, 10.23939/chcht16.03.440
31. M. K. Esmaeilzadeh and A. C. Najafi, DFT study on corrosion inhibition by tetrazole derivatives, *ACS Omega* **8** (2023) 9978, 10.1021/acsomega.2c07185
32. O. E. Oyeneyin *et al*., Corrosion inhibition potentials of indene derivatives: DFT and molecular dynamics, *Beni-Suef Univ. J. Basic Appl. Sci.* **11** (2022) 132, 10.1186/s43088-022-00313-0
33. R. Oukhrib *et al*., DFT, Monte Carlo and molecular dynamics simulations for prediction of corrosion inhibition efficiency, *Sci. Rep.* **11** (2021) 3771, 10.1038/s41598-021-82927-5
34. I. Lukovits, E. Kálmán, and F. Zucchi Corrosion inhibitors: correlation between electronic structure and efficiency *Corrosion* **57** (2001) 3, 10.5006/1.3290328
35. V. Saraswat, M. Yadav, and I. Obot, Eco-friendly corrosion inhibitors for mild steel in acid environment, *Colloids Surf. A* **599** (2020) 124881, 10.1016/j.colsurfa.2020.124881
36. S. Hadisaputra *et al*., Quantum chemical and Monte Carlo simulation studies on inhibition performance of caffeine derivatives, *Coatings* **10** (2020) 1086, 10.3390/coatings10111086
37. D. M. Mamand and H. M. Qadr, Corrosion inhibition efficiency and quantum chemical studies of organic compounds, *Corros. Rev.* **41** (2023) 427, 10.1515/corrrev-2022-0085
38. J. A. Rodriguez *et al*., Mathematical models for prediction of corrosion inhibition using theoretical chemistry simulations, *Materials* **13** (2020) 5656, 10.3390/ma13245656
39. X. Wang *et al*., Corrosion inhibition effect of benzimidazole and derivatives on copper in alkaline environments, *J. Mol. Liq.* **390** (2023) 122985, 10.1016/j.molliq.2023.122985
40. D. Sharma *et al*., Experimental and computational studies on corrosion inhibition potential of oxadiazole hybrid, *Environ. Sci. Pollut. Res.* **32** (2025) 17005, 10.1007/s11356-024-32678-3